npj | Quantum Information

www.nature.com/npjqi

ARTICLE OPEN

Inverted fine structure of a 6H-SiC qubit enabling robust spin-photon interface

I. D. Breev[1,2,6], Z. Shang[3,4,6], A. V. Poshakinskiy[1], H. Singh[5], Y. Berencén[3], M. Hollenbach[3,4], S. S. Nagalyuk[1], E. N. Mokhov[1], R. A. Babunts[1], P. G. Baranov[1], D. Suter[5], S. A. Tarasenko[1], G. V. Astakhov[3]✉ and A. N. Anisimov[1,2]✉

Controllable solid-state spin qubits are currently becoming useful building blocks for applied quantum technologies. Here, we demonstrate that in a specific type of silicon-vacancy in the 6H-SiC polytype the excited-state fine structure is inverted, compared to 4H-SiC. From the angular polarization dependencies of the emission, we reconstruct the spatial symmetry and determine the optical selection rules depending on the local deformation and spin–orbit interaction. We show that this system is well suited for the implementation of robust spin–photon entanglement schemes. Furthermore, the inverted fine structure leads to unexpected behavior of the spin readout contrast. It vanishes and recovers with lattice cooling due to two competing optical spin pumping mechanisms. Our experimental and theoretical approaches provide a deep insight into the optical and spin properties of atomic-scale qubits in SiC required for quantum communication and distributed quantum information processing.

npj Quantum Information (2022)8:23 ; https://doi.org/10.1038/s41534-022-00534-2

INTRODUCTION

Optically interfaced solid-state spins are considered as candidates for the realization of quantum networks and photonic quantum computing[1,2]. The practical realization of quantum repeaters requires a system with (i) a high-fidelity spin–photon interface, (ii) a source of spectrally indistinguishable single photons, and (iii) a long-lived quantum memory. One of the promising candidates is III–V semiconductor quantum dots (QDs)[3]. They are the brightest solid-state source of single photons in the telecom wavelength, which can be used for quantum key distribution. Due to the optical selection rules, there are robust, high-fidelity protocols for the entanglement generation between the photon polarization and the spin state. Yet, a short spin coherence time and a large inhomogeneous broadening of the emission wavelength from individual QDs are the main obstacles to their practical use. Another promising material platform is based on color centers in diamond. Indeed, high-fidelity (92%) entanglement at a distance of 1.3 km has been demonstrated with two nitrogen-vacancy (NV) centers in diamond[4]. The main obstacle for scaling up this system is its spectrally unstable emission, resulting in a very low entanglement generation rate. Another color center in diamond, the silicon-vacancy (SiV), is spectrally stable allowing memory-enhanced quantum communication protocols at mK temperatures[5].

There is a continuous search for other solid-state platforms for integrated quantum photonics with spin qubits. Silicon carbide (SiC) holds great promise as a technologically mature material[6–8]. Particularly, the negatively charged silicon-vacancy (V_{Si}) in SiC reveals appealing quantum properties[9,10]. They can be used as quantum emitters[11–13] and have an extremely long spin coherence time[12,14,15]. The V_{Si} centers can be naturally integrated into photonic structures[16–18] due to the established spin–photon interface[19,20] and high spectral stability of their zero-phonon lines (ZPLs)[21,22] along with nanoscale engineering of single V_{Si} with focused ion beams[23,24] and the ability for the Stark tuning of the V_{Si} ZPL[25,26]. These achievements pave the way for the on-demand generation of indistinguishable single-photon emitters. Furthermore, spin–photon entanglement schemes based on the excited-state (ES) fine structure and spin-dependent optical transitions to the ground state (GS) have been theoretically proposed[27,28] but not yet realized.

The most studied polytype is 4H-SiC, which is characterized by two non-equivalent lattice sites for Si. Correspondingly, there are two V_{Si} centers in 4H-SiC, which are historically labeled as V1 and V2. They differ from each other by their ZPL spectral position and zero-field splitting parameter $2D$[9,29]. It has also been established that the V1 ZPL in the low-temperature photoluminescence (PL) spectra split in two lines V1 and V1′, which are orthogonally polarized[29,30]. The dichroic properties of the V1/V1′ ZPL, as well as the V2 ZPL in 4H-SiC, have been recently investigated in detail[31]. Both the V1 ZPL, which dominates at low temperatures, and the V2 ZPL are linearly polarized along the *c*-axis of the 4H-SiC crystal, indicating that these centers emit light perpendicularly to the *c*-axis. Because the quantum-grade SiC epitaxial layers are usually grown along the *c*-axis, this makes light collection from the growth surface and, consequently, photon extraction from planar photonic structures less efficient. On the other hand, the fabrication of photonic structures from the side of the epitaxial layer is technologically laborious.

The polytype 6H-SiC has three non-equivalent lattice sites for Si, resulting in three V_{Si} centers. In the present paper, we perform a comprehensive study of these V_{Si} centers by polarization-resolved optical spectroscopy and optically detected magnetic resonance (ODMR) spectroscopy. The V1/V1′ and V2 centers in 6H-SiC have very similar properties to those in 4H-SiC. In contrast, the V3 center in 6H-SiC is optically active in two perpendicular polarizations and emits light preferentially along the *c*-axis, making the photon extraction from planar photonic structures easier. We explain this

---

[1]Ioffe Institute, Polytechnicheskaya 26, 194021 St. Petersburg, Russia. [2]Laboratory for diagnostics of carbon materials and spin-optical phenomena at wide-bandgap semiconductors, Northern (Arctic) Federal University, 163002 Arkhangelsk, Russia. [3]Helmholtz-Zentrum Dresden-Rossendorf, Institute of Ion Beam Physics and Materials Research, Bautzner Landstr. 400, 01328 Dresden, Germany. [4]Technische Universität Dresden, 01062 Dresden, Germany. [5]Fakultät Physik, Technische Universität Dortmund, 44221 Dortmund, Germany. [6]These authors contributed equally: I. D. Breev, Z. Shang. ✉email: g.astakhov@hzdr.de; aan0100@gmail.com

Published in partnership with The University of New South Wales

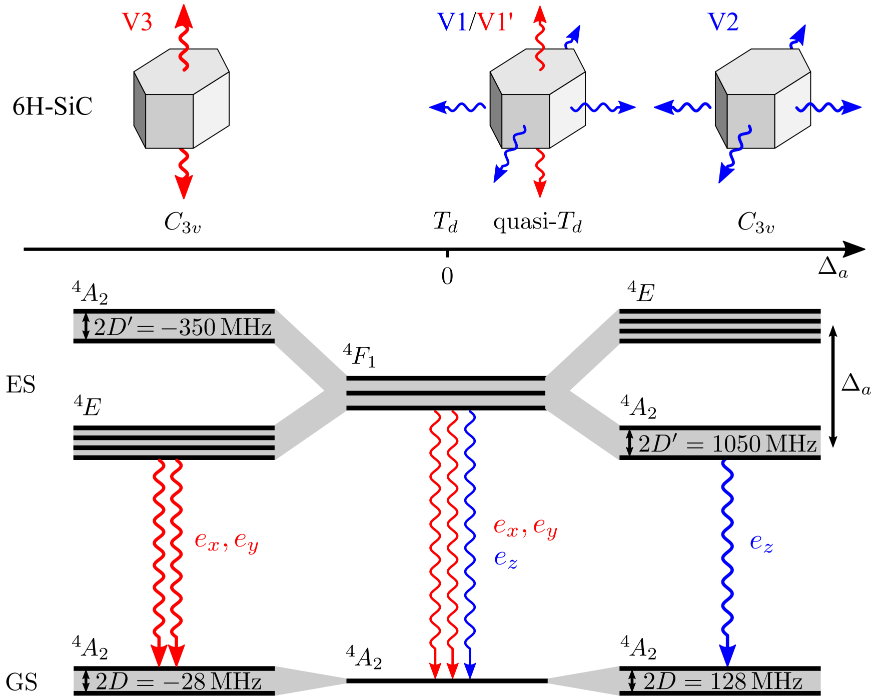

Fig. 1 Scheme of the V_{Si} ground state (GS) and excited-state (ES) multiplets. The polarized directional emission is linked to the ES structure in 6H-SiC. The zero-field splittings of the GS and ES $^4A_2$ octuplets for the V2 and V3 centers are obtained from the experiment as described in the text.

property by the inverted fine structure of the excited state with respect to other V_{Si} centres in 4H- and 6H-SiC. It also enables an entanglement scheme between the circular polarization of the emitted photon and the V_{Si} spin[28], which is not possible for the V1 or V2 centers. We also find that the V3 center has an unusual temperature-induced inversion of the ODMR signal at a critical point $T_c = 16$ K.

The V1/V1′, V2, and V3 centers differ by their deviation from the cubic symmetry T_d to the trigonal symmetry C_{3v}. This deviation can be characterized by the axial splitting Δ_a between the $^4A_2$ quadruplet and ^4E octuplet of the spin-3/2 ES, as depicted in Fig. 1. For cubic symmetry, $\Delta_a = 0$ and the excited state is then the 12-fold $^4F_1$ multiplet. For $\Delta_a \neq 0$, the $^4F_1$ multiplet splits into the $^4A_2$ quadruplet and ^4E octuplet, with the order being determined by the sign of Δ_a. Depending on what multiplet has the lowest energy, the PL of the center is polarized either along (e_z) or perpendicular (e_x, e_y) to the *c*-axis, as indicated by the wavy arrows in Fig. 1. As compared to V1 and V2, the V3 center has an inverted ES structure, which determines its unusual multipolarized (e_x, e_y) optical emission.

RESULTS

Inverted excited-state structure: experiment

First, we measure the orientation dependence of the polarization V_{Si} PL in 6H-SiC at room temperature (Fig. 2). The PL collected from the *n*-face, i.e., along the *c*-axis, is unpolarized (Fig. 2a). In contrast, the PL collected from the m-face, i.e., perpendicular to the *c*-axis, is partially polarized along the *c*-axis (Fig. 2b). At room temperature, the emission from the different V_{Si} centers overlap spectrally and it is not possible to distinguish between them. To separate spectral contributions from the different V_{Si} centers, we the microwave (MW) assisted spectroscopy[32]. Figure 2c and d presents ODMR spectra with a peak at 28 MHz corresponding to the V3 (probably also V1) V_{Si} centers and a negative peak at 128 MHz corresponding to the V2 V_{Si} center[9]. The V2 ΔPL/PL is clearly linearly polarized as $e_z||c$ (the inset of Fig. 2d). The polarization of the V3/V1 centers cannot be separated at room temperature and their cumulative contribution to the ΔPL/PL is preferentially polarized along the perpendicular direction as e_x, $e_y \perp c$.

At low temperature ($T = 15$ K), the V1, V2, and V3 V_{Si} centers in 6H-SiC are spectroscopically distinguishable by their ZPLs[29], as presented in Fig. 3a. We fit the angular dependencies from the m-face in Fig. 3b–d to

$$I_m(\varphi) = I_0(1 + \cos 2\theta \cos 2\varphi_m), \qquad (1)$$

where φ_m is the angle between the linear polarizer axis and the *c*-axis, I_0 is the average intensity. Phenomenologically, such a polarization dependence corresponds to the radiation of electric dipoles, d_x and d_z, oriented along and perpendicular to the *c*-axis, respectively. The parameter θ in Eq. (1) characterizes the ratio $|d_x|/|d_z| = \tan\theta$. Microscopically, the components of $\boldsymbol{d}$ can be calculated as the matrix elements of the electric dipole operator between the GS and the ES. It follows from the symmetry analysis that $d_x = d_y = 0$ and $d_z \neq 0$ for optical transitions from the pure $^4A_1$ ES ($\theta = 0°$) and $d_x = d_y \neq 0$ and $d_z = 0$ ($\theta = 90°$) for optical transitions from the pure ^{4}E ES.

The V1 ZPL shows nearly unpolarized emission (Fig. 3b) and a fit to Eq. (1) gives $\cos 2\theta = 0.06$ ($|d_x/d_z| \approx 0.94$). Earlier studies show that it consists of two, V1 and V1′ ZPLs, which are polarized as $e_z||c$ and $e_x, e_y \perp c$, respectively, and split by 1.1 meV, where V1′ is the high-energy state transition[30]. In our experiments, we do not resolve the V1 and V1′ ZPLs and therefore, the cumulative PL emission associated with the V1 V_{Si} center is nearly unpolarized.

After the background subtraction (Supplementary Information), the V2 ZPL shows nearly 100% polarization with $e_z||c$ (Fig. 3(c)). A fit to Eq. (1) gives $\cos 2\theta = 0.96$ ($\theta = 8° \approx 0°$). The V3 ZPL is orthogonally polarized $e_x, e_y \perp c$ with small but not vanishing contribution $e_z||c$ (Fig. 3d). A fit to Eq. (1) gives $\cos 2\theta = -0.89$ ($\theta = 76° \approx 90°$). We verify that the observed PL polarization does not

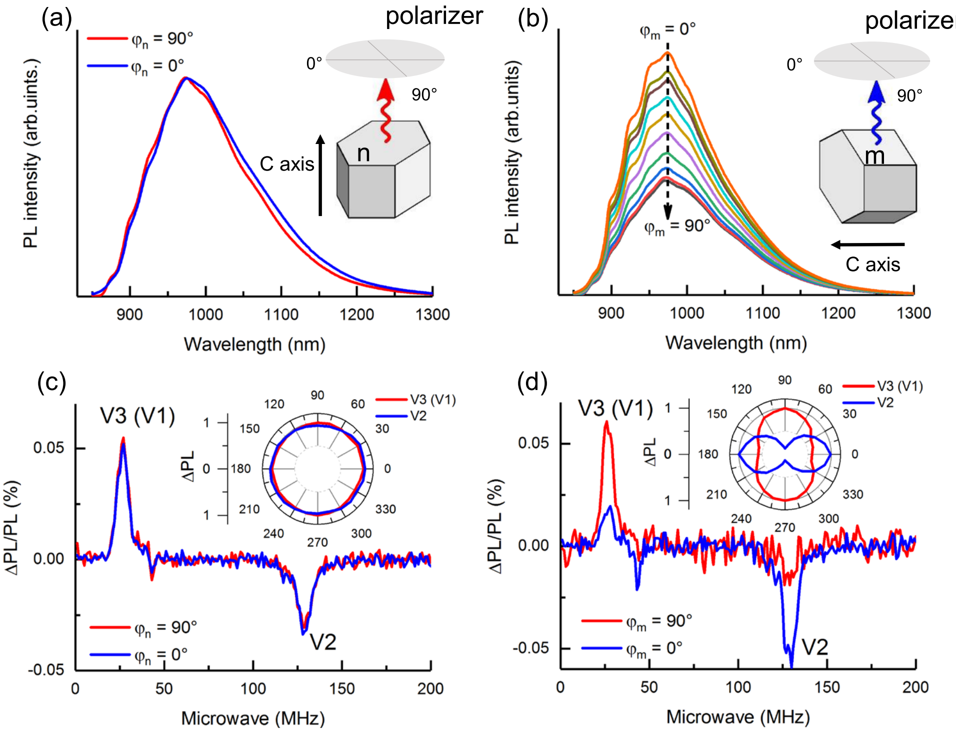

Fig. 2 Room-temperature polarization dependence of the V_{Si} PL in 6H-SiC. a, b PL spectra of V_{Si} centers taken from the *n*-face (perpendicular to the *c*-axis) and m-face (parallel to the *c*-axis), respectively, collected through the linear polarizer. The insets sketch the experimental geometries and the polarizer orientations. **c, d** ODMR spectra of the V3 (V1) and V2 V_{Si} centers at $\varphi_{n,m} = 0°$ (blue curve) and $\varphi_{n,m} = 90°$ (red curve) of the polarizer orientation. Insets: normalized polar plots $\Delta PL(\varphi_{n,m})$ for the *n*-face (**c**) and m-face (**d**), respectively.

depend on the excitation laser polarization (open and solid symbols in Fig. 3b–d). Furthermore, we observe nearly the same angular dependencies at a temperature $T = 100$ K (Supplementary Information), indicating that they are not related to the thermal population in the ES, which thus manifests intrinsic properties of the corresponding V_{Si} centers, as presented in Fig. 1.

Inverted excited-state structure: theory

Here, we construct the effective ES spin Hamiltonian, calculate the optical selection rules and compare them with the polarization dependencies observed in the experiments. The spatial symmetry of the vacancy-related spin centers in hexagonal SiC is described by the C_{3v} point group[33]. This group has one-dimensional irreducible representations A_1 and A_2 and a two-dimensional irreducible representation *E*. Therefore, all V_{Si} spin-3/2 spectral terms are either 4- or 8-fold multiplets. It is natural to assume that the V_{Si} GS in 6H-SiC is orbitally nondegenerate and corresponds to the $^4A_2$ quadruplet, similarly to the V_{Si} GS in 4H-SiC[27].

The low-temperature PL polarization is determined by the lowest ES multiple, which can be either $^4A_2$ quadruplet or ^{4}E octuplet[27]. The splitting between the $^4A_2$ and ^{4}E multiplets is caused by the distortion of the V_{Si} symmetry from the cubic T_d symmetry. In the T_d approximation, this splitting vanishes, and the $^4A_2$ quadruplet and the ^{4}E octuplet merge into the 12-fold $^4F_1$ multiplet of the T_d group, as shown in Fig. 1.

The ES-GS transitions $^4A_2 \rightarrow {}^4A_2$ are optically active in the polarization e_z ($z \| c$). The PL collected from the hexagonal *n*-plane should be quite weak, while the intensity of PL emitted from the side *m*-plane and transmitted through the polarizer should vary as $I \propto \cos^2\varphi_{\mathrm{m}}$. Such a polarization dependence is observed for the V2 ZPL (Figs. 2 and 3) and indicates that the lowest excited multiplet of the V2 center is $^4A_2$.

Contrary, the ES-GS transitions $^4E \rightarrow {}^4A_2$ are optically active in the e_x and e_y polarizations, which are perpendicular to the *c*-axis. The corresponding PL collected from the *n*-plane should be strong and unpolarized (at zero magnetic field) and the PL intensity collected from the *m*-plane through the polarizer should follow the φ-dependence $I \propto \sin^2\varphi_{\mathrm{m}}$. This polarization behavior is observed for the V3 ZPL, see Figs. 2 and 3. Therefore, we conclude that the ordering of the ES multiplets is inverted for the V3 center, with ^{4}E being the lowest multiplet.

The PL at the V1/V1′ ZPL is nearly unpolarized indicating that the $^4A_2$ and ^{4}E multiplets are close to each other and that the effective symmetry of the V_1 center is close to T_d, as shown in Fig. 1.

We note that the measured polarization dependencies at the V_2 and V_3 ZPLs are not as strict as the orbital symmetry suggests. This deviation can be attributed to the spin–orbit interaction or to a further distortion of the V_{Si} symmetry from C_{3v} due to local strain or the Jahn-Teller effect and will be discussed later.

To study the ES fine structure and the effect of strain, we construct now the effective Hamiltonian of the $^4A_2 + {}^4E$ states. These 12 states have angular momentum $L = 1$ and spin $S = 3/2$. The effective Hamiltonian can be expressed via the operators of the angular momenta $\boldsymbol{L}$ and $\boldsymbol{S}$

$$H = H_{\mathrm{e}} + H_{\mathrm{so}} + H_{\mathrm{ss}} + H_{\mathrm{def}}, \tag{2}$$

where the four terms correspond to the pure orbital, spin-orbital, spin–spin, and deformation interactions. The orbital term has the form

$$H_{\mathrm{e}} = \Delta_{\mathrm{a}}\left(L_z^2 - \frac{2}{3}\right) \tag{3}$$

and describes the splitting Δ_{a} between the ^4E octuplet (states with the eigenvalues $L_z = \pm 1$) and the $^4A_2$ quadruplet (states with the

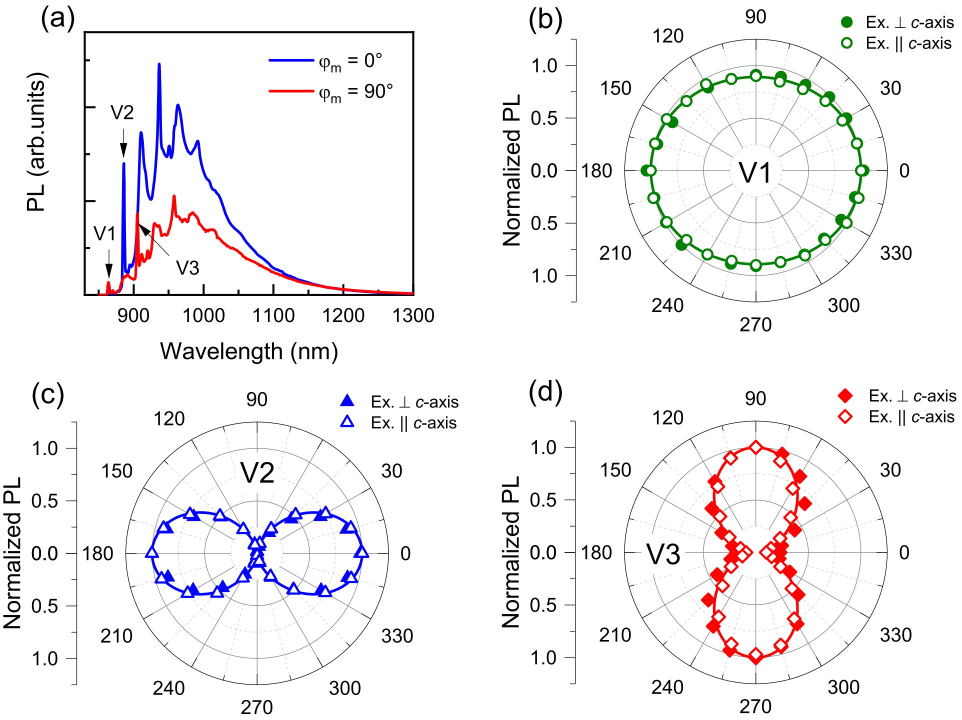

Fig. 3 **Polarization dependencies of the V_{Si} ZPLs in 6H-SiC at $T = 15$ K.** **a** PL spectra measured from the m-face at $\varphi_m = 0°$ (blue curve) and $\varphi_m = 90°$ (red curve) of the polarizer orientation with respect to the *c*-axis. **b–d** The polar polarization plots of the V1, V2, and V3 ZPL intensities, respectively. The solid and open symbols are the measured data for the excitation polarization perpendicular and parallel to the *c*-axis. The solid lines are fits to Eq. (1) with the fitting parameter $\cos 2\theta$ of 0.06, 0.96, and −0.89 for the V1, V2, and V3 ZPL, respectively.

eigenvalue $L_z = 0$ of). The spin–orbit interaction, linear in the spin operator $\boldsymbol{S}$, has the form

$$H_{\mathrm{so}} = \lambda \boldsymbol{L} \cdot \boldsymbol{S}\,, \tag{4}$$

where λ is the ES spin–orbit interaction constant. The spin–spin interaction, quadratic in the spin operators[34], is given by the sum of two terms

$$H_{\mathrm{ss}} = b\left[(\boldsymbol{S} \cdot \boldsymbol{L})^2 - \frac{5}{2}\right] + \tilde{D}\left(S_z^2 - \frac{5}{4}\right), \tag{5}$$

where b and $\tilde{D}$ are the spin–spin interaction parameters. Finally, the deformation mixing of orbital states is described by the Hamiltonian[35]

$$H_{\mathrm{def}} = \Xi_{\mathrm{e}} \sum_{\alpha\beta} \left(u_{\alpha\beta} - \frac{\delta_{\alpha\beta}}{3}\,\mathrm{Tr}\,u\right)\left(L_\alpha L_\beta - \frac{2}{3}\delta_{\alpha\beta}\right), \tag{6}$$

where Ξ_{e} is the deformation potential constant, $u_{\alpha\beta}$ is the strain tensor, and $\mathrm{Tr}\,u = \sum_\alpha u_{\alpha\alpha}$. The effect of strain on the spin–orbit and spin–spin interactions is much smaller and neglected here. To avoid the multiplication of parameters, all the contributions to the Hamiltonian (2) are given in the isotropic approximation except for the terms $(L_z^2 - 2/3)$ and $(S_z^2 - 5/4)$, which vanish in the isotropic model and take into account the axial symmetry.

We assume the following energy hierarchy: $\Delta_{\mathrm{a}} \gg \lambda \gg b, \tilde{D}$ and $\Delta_{\mathrm{a}} \gg \Xi_{\mathrm{e}} u_{\alpha\beta}$. Then, using the Löwdin perturbation theory[36], we obtain the effective Hamiltonian of the ${}^4A_2$ quadruplet

$$H_{A_2} = \varepsilon_{A_2} + D'\left(S_z^2 - \frac{5}{4}\right), \tag{7}$$

where $\varepsilon_{A_2} \approx -(2/3)\Delta_{\mathrm{a}}$ is the quadruplet position and $2D'$ is the zero-field splitting between the ±1/2 and ±3/2 spin sublevels of the ${}^4A_2$ ES quadruplet. For the first order in the spin–spin interaction and the second order in the spin–orbit interaction, the zero-field splitting constant has the form

$$D' = \tilde{D} - b + \frac{\lambda^2}{\Delta_{\mathrm{a}}}, \tag{8}$$

for the ^{4}E octuplet the Löwdin perturbation theory gives the effective Hamiltonian

$$\begin{aligned} H_{\mathrm{E}} = {} & \varepsilon_{\mathrm{E}} + \lambda S_z \sigma_z + D''\left(S_z^2 - \tfrac{5}{4}\right) \\ & + D''_{\perp}\left[(S_x^2 - S_y^2)\sigma_x + (S_x S_y + S_y S_x)\sigma_y\right] \\ & + \tfrac{1}{2}\Xi_{\mathrm{e}}\left[(u_{xx} - u_{yy})\sigma_x + 2u_{xy}\sigma_y\right], \end{aligned} \tag{9}$$

where $\varepsilon_{\mathrm{E}} \approx \Delta_{\mathrm{a}}/3$ is the octuplet position, σ_x, σ_y, and σ_z are the Pauli matrices in the space of orbital states with $L_z = \pm 1$,

$$D'' = \tilde{D} + \frac{b}{2} - \frac{\lambda^2}{2\Delta_{\mathrm{a}}}\,, \tag{10}$$

$$D''_{\perp} = \frac{b}{2} + \frac{\lambda^2}{2\Delta_{\mathrm{a}}}. \tag{11}$$

Figure 4a shows schematically the GS and ES multiplet structure in the absence of strain. For $\Delta_{\mathrm{a}} < 0$, which corresponds to the V3 center, the ${}^4E$ octuplet is below the ${}^4A_2$ quadruplet in the ES. The spin–orbit and spin–spin interactions form the fine structure of the multiplets. We cannot determine the dominant contribution to the ${}^4E$ octuplet splitting from our experimental data. According to DFT calculations, the spin–orbit interaction constant is $\lambda/h \sim 100$ GHz for the V2 V_{Si} in 4H-SiC[37]. Another estimate gives $\lambda/h \sim 5$ GHz[28]. The spin–orbit and deformation interactions not only determine the fine structures of the ^{4}E and ${}^4A_2$ multiplets but also mix them. Figure 4b shows the ES structure as a function of the spin–orbit interaction strength λ in the presence of a small shear strain u_{xz}. The energy levels are calculated numerically by the direct diagonalization of Hamiltonian (2). When λ becomes comparable to the splitting between the multiplets Δ_{a}, they get fully mixed. Figure 4c shows the ES structure as a function of the shear strain

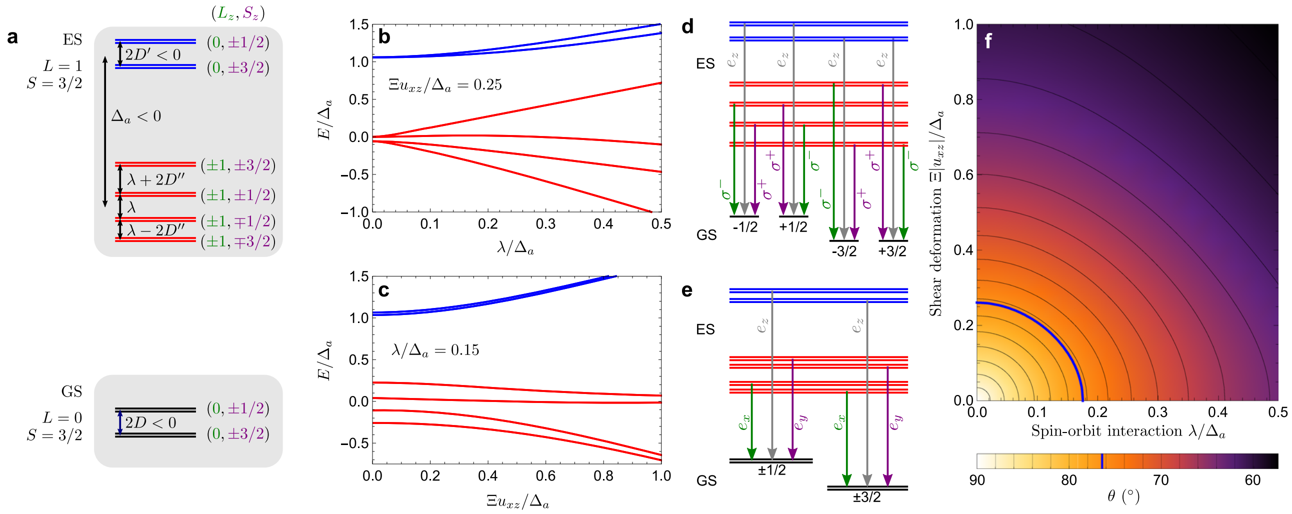

Fig. 4 Ground state (GS) and excited states (ES) fine structure of the V3 V_{Si} center in 6H-SiC. a Schematic presentation of the GS and ES spin sublevels depending on L_z and S_z. **b** Dependence of the ES spin sublevels on the spin–orbit interaction strength λ in the presence of shear strain $\Xi u_{xz}/\Delta_a = 0.25$. **c** Dependence of the ES spin sublevels on the shear strain u_{xz} in the presence of spin–orbit interaction $\lambda/\Delta_a = 0.15$. **d, e** Selection rules for the optical transitions between the ES and GS levels shown for the cases of **d** dominant spin–orbit interaction and **e** dominant deformation coupling. **f** Color plot of the angle $\theta = \arctan(|d_x/d_z|)$, describing the PL polarization at the transitions from the ^4E ES multiplet to the GS, as a function of the spin–orbit interaction strength λ and the shear strain u_{xz}. The thick line indicates the angle $\theta = 76^\circ$ measured for the V3 center in our experiments.

u_{xz}. The deformation coupling of different orbital states suppresses spin–orbit splitting. When $\Xi^2 u_{xz}^2/\Delta_a >> \lambda$, the ^{4}E octuplet transforms into a pair of quadruplets.

Next, we analyze the polarization of the electric dipole optical transitions between the ES and GS. In the case of negligible mixing of the ES multiplets, the transitions from the $^4A_2$ quadruplet are active in the e_z polarization while the transitions from the ^{4}E octuplet are active in the e_x and e_y polarizations. The selection rules for the transitions between particular levels of the ^{4}E ES octuplet and the $^4A_2$ GS quadruplet are determined by the fine structures of the multiplets. If the spin–orbit interaction dominates, $\lambda \gg \Xi u_{xz}$, these transitions are active in the polarizations $(e_x \pm i e_y)/\sqrt{2}$ and occur with the emission of circularly polarized photons, as depicted in Fig. 4d. If the deformation interaction induced by shear strain dominates, $\Xi u_{xz} \gg \lambda$, the emitted photons are linearly polarized, Fig. 4e.

The strict selection rules, which imply that the optical transitions from the $^4A_2$ and the ^{4}E states are active in the polarization parallel and perpendicular to the *c*-axis, respectively, are violated if the multiplets are mixed. To study this violation, we calculate the phenomenological tilt angle of the electric dipole $\theta = \arctan|d_x/d_z|$, which determines the PL polarization, taking into account the mixing of the multiplets by the spin–orbit interaction and strain. We assume that the distortion of the T_d symmetry is small, so the d_z matrix element between the pure $^4A_2$ ES and the GS is equal to d_x and d_y between the pure ^{4}E ES and the GS. Figure 4f shows the angle θ for the optical transitions from the ^{4}E multiplet as a function of the parameters λ/Δ_a and $\Xi u_{xz}/\Delta_a$. The thick solid curve corresponds to the value $\theta_E = 76^\circ$ observed in our experiment for the V3 centers (Fig. 3d). In the case of weak mixing of the multiplets, $\Xi u_{xz}, \Xi u_{yz}, \lambda \ll \Delta_a$, the dipole angles for the transitions from the $^4A_2$ and the ^{4}E states have the form

$$\theta_{A_2} \approx \frac{\sqrt{\frac{\Xi^2}{2}(u_{xz}^2 + u_{yz}^2) + \frac{5}{4}\lambda^2}}{\Delta_a}, \tag{12}$$

$$\theta_E \approx \frac{\pi}{2} - \frac{\sqrt{\Xi^2(u_{xz}^2 + u_{yz}^2) + \frac{5}{2}\lambda^2}}{\Delta_a}. \tag{13}$$

The value $\theta_E = 76^\circ$ can be explained by the spin–orbit interaction with $\lambda/\Delta_a \approx 0.18$, the shear strain with $\Xi\sqrt{u_{xz}^2 + u_{yz}^2}/\Delta_a \approx 0.26$, or by the combination of both effects.

With increasing temperature, both the $^4A_2$ and ^{4}E multiplets get thermally populated leading to a reduction of the PL polarization. This depolarization is observed by the comparison between Figs. 2d and 3c, d. At room temperature of Fig. 2(d), the ratio $\cos 2\theta$ is reduced from 0.96 to 0.72 for the V2 centers and from −0.89 to −0.26 for the V3 centers. This allows us to estimate the energy separation between the multiplets $\Delta_a \approx 60$ meV and $\Delta_a \approx -20$ meV for the V2 and V3 centers, respectively (Supplementary Information).

Excited-state level anticrossing

To experimentally probe the fine structure of the spin multiplets, we apply external magnetic fields B along the *c*-axis and study how it affects the PL signal. At certain values of B, determined by the zero-field splitting, level anticrossing (LAC) between a pair of spin states occurs[33]. At these four magnetic fields, corresponding to two ES level anticrossing (ESLAC) and two GS level anticrossing (GSLAC), the spin states are mixed resulting in a resonant change of the PL intensity[38,39]. The shape of the PL intensity in the vicinity of LAC is determined by the parity and spin dynamics of the corresponding spin levels[40,41]. Figure 5 shows the magnetic field dependence of the PL for two temperatures. The narrow GSLAC resonances at low magnetic fields allow us to determine the GS zero-field splitting $2D$[33]. The broader ESLAC resonances show clear temperature dependence and we determine the ES zero-field splitting $2D'$ together with the thermal shift $\beta = 2dD'/dT$[38]. All these parameters are summarized in Table 1.

Surprisingly, the V3 ESLACs in Fig. 5 have small amplitude but are clearly observed even though the $^4A_2$ quadruplet lies energetically higher than the ^{4}E octuplet due to the V3 inverted ES structure (Fig. 1). A possible reason is that for non-resonant excitation the V3 centers reside in the $^4A_2$ state for some time during the excitation-relaxation cycle[42]. Note that the ESLACs in the ^{4}E octuplet are expected at much higher magnetic fields than those used in our experiments. Furthermore, we find that the V3

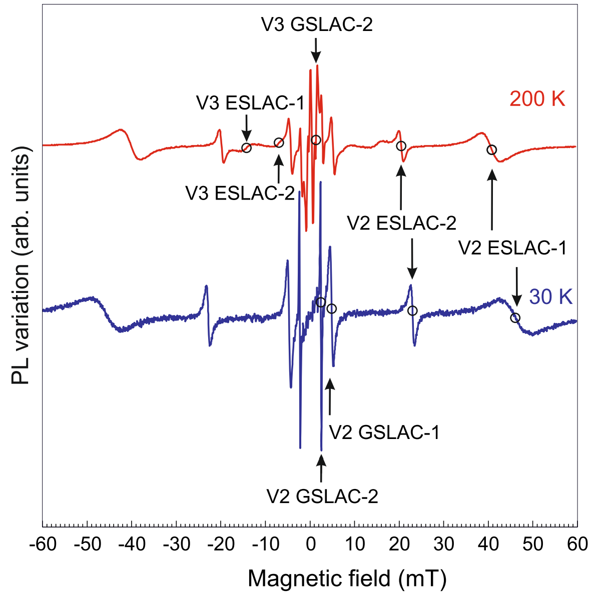

Fig. 5 PL intensity variation with magnetic field. The arrows indicate the GSLAC and ESLAC for the V3 (left part) and V2 (right part).

Table 1. Temperature dependence of the zero-field splitting in the GS ($2D$) and ES ($2D'$).

Center	$2D$	$2D'$ @ 300 K	β @ 300 K
V2	128 MHz	1050 MHz	−1.16 MHz/K
V3	−28 MHz	−350 MHz	0.84 MHz/K

The temperature shift is obtained as $\beta = 2\,dD'/dT$ at room temperature from the ESLAC[38].

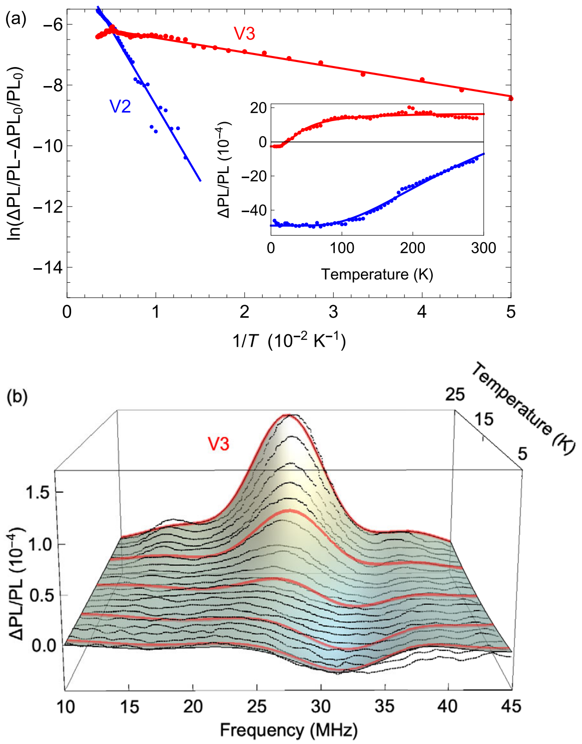

Fig. 6 Dependence of the ODMR signal on temperature. a Arrhenius plot of the ODMR signal for V2 and V3 centers. The plot was obtained from the ODMR temperature dependencies (inset) after subtracting the constant background $\Delta PL_0/PL_0$ corresponding to ODMR at $T = 0$. **b** Temperature variation of the ODMR signal for the V3 center in the vicinity of the critical temperature, where the sign changes. Dots are the experimental data, the surface and the red lines are the result of the fit after Eq. (16). The best fit is obtained with the critical temperature $T_c = 16$ K and $\gamma = 1.4$ K/MHz.

GSLAC and ESLAC resonances disappear at lower temperatures (Fig. 5), indicating that the optical spin pumping mechanism becomes inefficient at certain temperatures.

Temperature inversion of the ODMR signal

To understand the effect of temperature on the spin properties, we measure ODMR spectra in the range of 5–300 K (Fig. 6). The Arrhenius plot of Fig. 6a reveals an activation-law behavior for both, the V2 and V3 centers with activation energies of 43 and 4.1 meV, respectively. These values are in agreement, within an order of magnitude, with the values obtained from the polarization dependencies and might be associated with the thermal activation of either ^4E or $^4A_2$ ES in the case of the V2 or V3 center, respectively.

As shown in the inset of Fig. 6a, the ODMR contrast for the V2 center has a large negative offset $\Delta PL_0/PL_0 = -5 \times 10^{-3}$ at $T = 0$ and remains negative at all temperatures. Interestingly, the offset for the V3 center $\Delta PL_0/PL_0 = -5 \times 10^{-4}$ at $T = 0$ is much smaller. As a result, the ODMR signal for the V3 center changes sign at a critical temperature T_c.

Figure 6a shows the ODMR spectra in the vicinity of T_c for the frequency range of the V3 GS resonance. As the temperature drops below 20 K, the ODMR signal decreases, and the resonance lineshape becomes strongly asymmetric. Below 10 K, the resonance assumes again a symmetric shape but its sign is now negative. The PL intensity (not shown) remains almost constant at the same time. We also study the variation of the electronic paramagnetic resonance (EPR) of the V3 center with temperature, which follows exactly the same behavior (Supplementary Information).

To describe the temperature variation of the ODMR lineshape in the vicinity of T_c, we assume that the optically induced spin quadrupole polarization of the V3 center d_0[40] is determined by two competing mechanisms, which compensate each other at the critical temperature T_c. In the vicinity of this critical temperature, the spin polarization increases linearly as

$$d_0(T) \propto T - T_c\,. \tag{14}$$

In an inhomogeneously broadened ensemble with a variation of the zero-field splitting $2D$, the critical temperature T_c also varies. We suppose that since both variations are likely to be caused by local deformations[43], so there exists a correlation

$$T_c - T_c^{(0)} = \gamma\left(D - D^{(0)}\right) \tag{15}$$

where $T_c^{(0)}$ and $D^{(0)}$ are the average values of the zero-field splitting constant and the critical temperature in the ensemble, respectively, and γ is a constant. Then, the ODMR signal becomes

$$\Delta PL(\nu) \propto \left[T - T_c^{(0)} - \gamma\left(\frac{h\nu}{2} - D^{(0)}\right)\right] \exp\left[-\frac{\left(h\nu/2 - D^{(0)}\right)^2}{2(\delta D)^2}\right] \tag{16}$$

where $(\delta D)^2$ is the variance of the zero-field splitting constant. We use Eq. (16) to model the experimental ODMR spectra. From the best fits in Fig. 6(a), we determine the critical temperature $T_c = 16$ K.

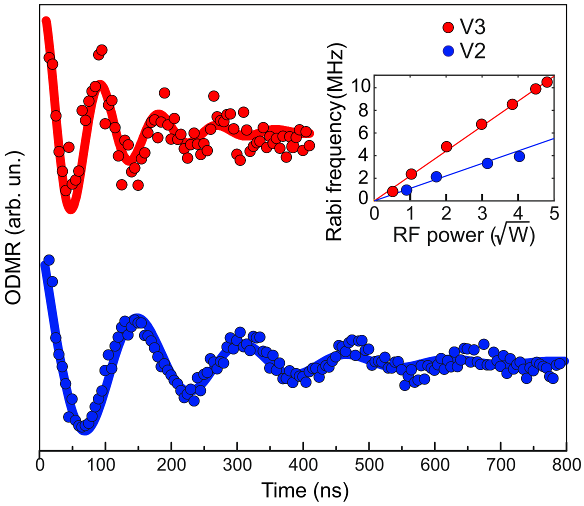

Fig. 7 Rabi oscillations. Rabi oscillations recorded at 5K for the V2 and V3 centers. Symbols are experimental data and solid lines are fits to Eq. (17). Inset: Rabi oscillation frequency as a function of the MW power.

Rabi oscillations

For quantum spin-photonic applications, it is important to demonstrate the coherent control of the V3 center at low temperatures below T_c. Figure 7 shows Rabi oscillations of the V3 spin, which is recorded at the optimal MW frequency of 32 MHz at $T = 5$ K according to Fig. 6a along with a power of 26 W. For comparison, we also measure Rabi oscillations for the V2 spin with the conventional ES structure at the same temperature. In this case, we use a MW frequency of 128 MHz with a power of 20 W, which equals the V2 spin resonance. The experimental data are well fitted to a function

$$S_{\mathrm{MW}}(\tau) - S_0(\tau) = A + B\cos(\omega\tau + \phi)\, e^{-\tau/T_2^*}\,, \qquad (17)$$

where S_{MW} and S_0 are the averaged PL signals measured with and without MW pulse, respectively. The obtained inhomogeneous dephasing times T_2^* are 219 ± 16 ns 129 ± 20 ns for the V2 and V3 ceneters, respectively. These times are similar to earlier reported values for room-temperature experiments in 6H-SiC[44–46].

DISCUSSION

The exact values of the spin–orbit interaction and the local deformation are not determined in our experiments. They should be performed on single V3 centers using polarization-resolved PL excitation spectroscopy[22], which is beyond the scope of this work. Here, we discuss the spin–photon interface for two limits, $\lambda \gg \Xi u_{xz}$ and $\lambda \ll \Xi u_{xz}$.

The optical selection rules for the dominant spin–orbit interaction are presented in Fig. 4d. Particularly, the optical transitions from the lowest, two-fold degenerate ES have the same energy and are circularly polarized $\sigma^{\pm}$ depending on the final GS $|\mp 3/2\rangle$. This II-system has some similarities to the trion spin states[47] and optical selection rules in semiconductor quantum dots, suggested for the implementation of quantum repeaters[3]. One of the robust quantum repeater schemes makes use of the entanglement between the spin state and photon polarization. The entanglement protocol consists of several well-documented steps[48]. First, the system is initialized into the $|+3/2\rangle$ GS state using resonant GS-ES optical excitation together with a resonant $(-3/2 \to -1/2)$ MW field[19]. Then, the superposition $|+3/2\rangle + |-3/2\rangle$ is created by applying a sequence of $\pi/2$ and π MW pulses to the dipole-allowed transitions in the GS[15]. Finally, a resonant excitation into the ES with the optical π pulse followed by the spontaneous emission generates the spin–photon entangled state $|\sigma^-\rangle|+3/2\rangle + |\sigma^+\rangle|-3/2\rangle$.

In case of the dominant deformation coupling shown in Fig. 4e, the lowest ES state is four-fold degenerate. The optical transitions from this state to the $|\pm 1/2\rangle$ and $|\pm 3/2\rangle$ GS are linearly polarized, e.g., e_x, and differ in their emission wavelength. This case can also be extended to the spontaneous deformation in the ES due to the Jahn-Teller effect with random linear polarization $e_{x,y}$ of the emission. Such a Λ-system bears some analogies to the silicon-vacancy center in diamond. It enables memory-enhanced quantum communication and realization of heralded spin–photon gates[5].

The practical implementation of spin–photon repeaters requires indistinguishability of the emitted photons and their high emission rate. The former can be realized with the Stark tuning[25,26]. The demonstrated high spectral stability of the V1/V2 centers in SiC in the earlier works[21,22] is caused by the identical $^4A_2$ symmetry in the GS and lowest ES[20], which is not the case for the inverted ES structure. Therefore, the spectral stability of single V3 centers should be benchmarked in future experiments. On the other hand, spectral diffusion can be suppressed using charge depletion in p-i-n structures[49]. An improvement of almost two orders of magnitude of the V1/V2 ZPL has been demonstrated by coupling them into photonic structures[16–18]. In these experiments, photon collection is performed along the *c*-axis, which is unfavorable for the V1 and V2 centers. Given the directional emission of the V3 center along the *c*-axis, we expect even a higher photon extraction rate.

In summary, we report the inverted structure of the excited states of the V3 V_{Si}-center in 6H-SiC, leading to the unusual temperature behavior of the optical spin pumping. By combining an experimental study with a theoretical model, we establish the selection rules for all-optical transitions. It results in the multi-polarized directional emission with favorable orientation for the photon extraction from photonic structures. Furthermore, the inverted ES structure enables robust spin–photon entanglement protocols, which are essential for quantum networks. Our findings demonstrate that the V3 V_{Si} in 6H-SiC is a promising spin center for quantum applications, which should stimulate further development of other non-conventional SiC polytypes as a material platform for wafer-scale quantum technology.

METHODS

Growth technique

The 6H-SiC crystals are grown by physical vapor deposition with on-axis orientation. The micropore density is about 5 cm^{-2} and the residual dopant concentration below 1×10^{17} cm^{-3}. The original crystal (3 inches diameter and 100 mm in thik) is diced in rectangular parallelepipeds with a thickness along the *c*-axis of 1.15 mm and a base of 2.3 × 2.3 mm^2. After dicing, all six surfaces of the sample are grounded and polished using a diamond slurry. To create V_{Si}, electron irradiation with an energy of 2 MeV to a fluence of 1×10^{18} cm^{-2} is performed throughout the entire volume of the samples.

ODMR technique

Setup used for the cw- and time-resolved ODMR measurements show in Supplementary Fig. 1. For cooling the sample, we used a liquid helium flow cryostat (MicrostatHe-R from Oxford instruments). Used a turbopump for creating a vacuum in the cryostat pressure less than 10^{-6} mbar (Pfeiffer). Used a 785 nm diode laser as our light source (Thorlabs LD785-SE400), a laser diode controller (LDC202C series), and a temperature controller (TED 200C)). An acousto-optical modulator (NEC model OD8813A) was used for creating the laser light pulses. For applying the static magnetic field to the sample, we used three orthogonal coil-pairs. The PL signal was recorded with an avalanche photodiode (APD) module (C12703 series from Hamamatsu). The signal from the APD was recorded with the USB oscilloscope card (PicoScope 2000 series) during pulse mode ODMR experiments. For cw-ODMR, the signal from APD was recorded with the lock-in (SR830 DSP). For cw-ODMR experiments as an RF source, we used a direct digital synthesizer (DDS AD9915 from Analog Devices). For pulsed ODMR experiments, we used an arbitrary wave generator (AWG DAx14000 from Hunter Micro). An RF signal from the source was amplified using an RF amplifier (LZY-22+ from mini circuits). Was used a digital word generator to generate TTL-pulses (PulseBlaster ESR-PRO PCI card). The RF to the sample was applied in the CW experiments using a 50 µm wire terminated by a 50 Ohm resistor placed over the sample. For the pulsed mode ODMR experiments, an RF pulse was applied to the sample through a handmade Helmholtz-pair of RF coils with 2.5 mm diameter and 6 turns in each coil from 100 µm diameter wire terminated with a 50 Ohm resistor.

To measure Rabi oscillations, the laser pulse with a duration of 20 ms and a power of 38 mW is used to initialize the V_{Si} spins. It is followed by a MW pulse of variable duration applied to the sample through Helmholtz coils, producing AC magnetic fields perpendicular to the *c*-axis of the crystal. The PL signal is recorded by the second laser pulse with a duration 16 µs. For reference, we repeat the same sequence except for the RF pulse. The reference is subtracted from the signal to eliminate the background.

Angular-dependence measurements

When the PL signal passes through optical components (such as monochromator), there is a polarization-dependent intensity loss. Therefore, we perform the calibration of the angular-dependent detection sensitivity as shown schematically in Supplementary Fig. 2(a). The PL intensity $I_{\rm meas}$ of the unpolarized signal $I_{\rm PL}$ depends on the angle α between the axis of the linear polarizator and the certain direction (for instance, defined by the monochromator slit) as

$$I_{\rm meas} = I_{\rm PL}(1 + A - A\cos 2\alpha)\,. \tag{18}$$

Here, $1 + 2A$ is the correction factor due to the different sensitivity for $\alpha = 0°$ and $\alpha = 90°$. To take into account the possible intrinsic PL polarization, we perform measurements for two sample orientations with $\beta = 0°$ and $\beta = 90°$ as presented in Supplementary Fig. 2(b). The correction factor for different wavelengths (λ) is obtained as

$$1 + 2A(\lambda) = \frac{I_{0^\circ,90^\circ}(\lambda) + I_{90^\circ,90^\circ}(\lambda)}{I_{0^\circ,0^\circ}(\lambda) + I_{90^\circ,0^\circ}(\lambda)}\,, \tag{19}$$

where $I_{\beta,\alpha}(\lambda)$ is the PL intensity for the given orientations of the sample (β) and polarizer (α) at a wavelngth λ. To obtain the angular dependences of the PL signal $I_{\rm PL}(\alpha)$, the measured intensities $I_{\rm meas}(\alpha)$ are corrected for each λ using Eq. (18).

Supplementary Fig. 3 presents polar plots of the V_{Si} in 6H-SiC obtained by two alternative approaches. In the first approach, we use the MW-assisted spectroscopy, which allows to separate overlapping contributions from different color centers[32]. The angular-dependence measurements are presented in Supplementary Fig. 3(b) and (c) at a temperature $T = 100$ K. There are clear angular dependencies of the V2 and V3 V_{Si} centers, with orthogonally oriented polar plots. In the second approach, we measure the ZPL intensity and subtract the PSB contribution from other centers as presented in Supplementary Fig. 3(d)–(f) for the V1, V2, and V3 ZPLs, respectively. Both approaches give the same results.

Further validation is presented in Supplementary Fig. 4 for lower temperature $T = 100$ K. In case V1, the $\rm ZPL_{V1}$ angular-dependent can be directly obtained from the low-temperature PL spectra (Supplementary Fig. 4(a)) because there is no contribution from the V2 or V3 ZPLs (Supplementary Fig. 4(c)). The PL intensity at the V2 ZPL includes two contributions, the V2 ZPL and the V1 PSB

$$\rm ZPL_{V2} = PL_{atZPL_{V2}} - PSB_{V1atZPL_{V2}}\,. \tag{20}$$

We assume that the ratio $a = \rm ZPL/PSB$ is polarization-independent and Eq. (20) can be rewritten as

$$\rm ZPL_{V2} = PL_{atZPL_{V2}} - \mathit{a}ZPL_{V1}\,. \tag{21}$$

The parameter a is obtained from the PL spectrum at $\varphi_m = 90°$, when the contribution from the V2 ZPL is negligible (Supplementary Fig. 4(b)). The V2 angular dependence before and after the PSB subtraction is presented in Supplementary Fig. 4(d). Similarly, the PL intensity at the V3 ZPL includes three contributions, the V3 ZPL, the V1 PSB, and the V2 PSB, which can be rewritten as

$$\rm ZPL_{V3} = PL_{atZPL_{V3}} - \mathit{b}ZPL_{V1} - \mathit{c}ZPL_{V2}\,. \tag{22}$$

The parameters b and c are obtained from the PL spectra of Supplementary Fig. 4(b) at $\varphi_m = 90°$ and $\varphi_m = 0°$, respectively. The V3 angular dependence before and after the PSB subtraction is presented in Supplementary Fig. 4(e).

DATA AVAILABILITY

The experimental data are available upon reasonable request.

CODE AVAILABILITY

The code to preprocess the dataset and analyze the experimental results is available from the corresponding author on reasonable request.

Received: 24 August 2021; Accepted: 26 January 2022;
Published online: 03 March 2022

REFERENCES

1. Atatüre, M., Englund, D., Vamivakas, N., Lee, S.-Y. & Wrachtrup, J. Material platforms for spin-based photonic quantum technologies. *Nat. Rev. Mater.* **3**, 38–51 (2018).
2. Awschalom, D. D., Hanson, R., Wrachtrup, J. & Zhou, B. B. Quantum technologies with optically interfaced solid-state spins. *Nat. Photonics* **12**, 516–527 (2018).
3. De Greve, K. & Yamamoto, Y. *Spin-Photon Entanglement in Semiconductor Quantum Dots: Towards Solid-State-Based Quantum Repeaters*, 71–89 (Springer Japan, 2016).
4. Hensen, B. et al. Loophole-free bell inequality violation using electron spins separated by 1.3 kilometres. *Nature* **526**, 682–686 (2015).
5. Bhaskar, M. K. et al. Experimental demonstration of memory-enhanced quantum communication. *Nature* **580**, 60–64 (2020).
6. Castelletto, S. & Boretti, A. Silicon carbide color centers for quantum applications. *J. Phys. Photonics* **2**, 022001 (2020).
7. Lukin, D. M., Guidry, M. A. & Vučković, J. Integrated quantum photonics with silicon carbide: challenges and prospects. *PRX Quantum* **1**, 020102 (2020).
8. Son, N. T. et al. Developing silicon carbide for quantum spintronics. *Appl. Phys. Lett.* **116**, 190501 (2020).
9. Baranov, P. G. et al. Silicon vacancy in SiC as a promising quantum system for single-defect and single-photon spectroscopy. *Phys. Rev. B* **83**, 125203 (2011).
10. Riedel, D. et al. Resonant addressing and manipulation of silicon vacancy qubits in silicon carbide. *Phys. Rev. Lett.* **109**, 226402 (2012).
11. Kraus, H. et al. Room-temperature quantum microwave emitters based on spin defects in silicon carbide. *Nat. Phys.* **10**, 157–162 (2014).
12. Widmann, M. et al. Coherent control of single spins in silicon carbide at room temperature. *Nat. Mater.* **14**, 164–168 (2015).
13. Fuchs, F. et al. Engineering near-infrared single-photon emitters with optically active spins in ultrapure silicon carbide. *Nat. Commun.* **6**, 7578 (2015).
14. Simin, D. et al. Locking of electron spin coherence above 20 ms in natural silicon carbide. *Phys. Rev. B* **95**, 161201(R) (2017).
15. Soltamov, V. A. et al. Excitation and coherent control of spin qudit modes in silicon carbide at room temperature. *Nat. Commun.* **10**, 1678 (2019).
16. Radulaski, M. et al. Scalable quantum photonics with single color centers in silicon carbide. *Nano Lett.* **17**, 1782–1786 (2017).
17. Bracher, D. O., Zhang, X. & Hu, E. L. Selective Purcell enhancement of two closely linked zero-phonon transitions of a silicon carbide color center. *Proc. Natl Acad. Sci. USA* **114**, 4060–4065 (2017).
18. Lukin, D. M. et al. 4H-silicon-carbide-on-insulator for integrated quantum and nonlinear photonics. *Nat. Photonics* **14**, 330–334 (2020).
19. Nagy, R. et al. High-fidelity spin and optical control of single silicon-vacancy centres in silicon carbide. *Nat. Commun.* **10**, 1954 (2019).
20. Udvarhelyi, P. et al. Spectrally stable defect qubits with no inversion symmetry for robust spin-to-photon interface. *Phys. Rev. Appl.* **11**, 044022 (2019).
21. Banks, H. B. et al. Resonant optical spin initialization and readout of single silicon vacancies in 4H-SiC. *Phys. Rev. Appl.* **11**, 024013 (2019).
22. Morioka, N. et al. Spin-controlled generation of indistinguishable and distinguishable photons from silicon vacancy centres in silicon carbide. *Nat. Commun.* **11**, 2516 (2020).
23. Kraus, H. et al. Three-dimensional proton beam writing of optically active coherent vacancy spins in silicon carbide. *Nano Lett.* **17**, 2865–2870 (2017).
24. Wang, J. et al. Scalable fabrication of single silicon vacancy defect arrays in silicon carbide using focused ion beam. *ACS Photonics* **4**, 1054–1059 (2017).
25. Rühl, M., Bergmann, L., Krieger, M. & Weber, H. B. Stark tuning of the silicon vacancy in silicon carbide. *Nano Lett.* **20**, 658–663 (2020).

26. Lukin, D. M. et al. Spectrally reconfigurable quantum emitters enabled by optimized fast modulation. *npj Quantum Inf.* **6**, 687–689 (2020).
27. Soykal, Ö. O., Dev, P. & Economou, S. E. Silicon vacancy center in 4H-SiC: electronic structure and spin-photon interfaces. *Phys. Rev. B* **93**, 081207 (2016).
28. Economou, S. E. & Dev, P. Spin-photon entanglement interfaces in silicon carbide defect centers. *Nanotechnology* **27**, 504001 (2016).
29. Wagner, M. et al. Electronic structure of the neutral silicon vacancy in 4H and 6H SiC. *Phys. Rev. B* **62**, 16555–16560 (2000).
30. Janzén, E. et al. The silicon vacancy in SiC. *Phys. B Condens. Matter* **404**, 4354–4358 (2009).
31. Nagy, R. et al. Quantum properties of dichroic silicon vacancies in silicon carbide. *Phys. Rev. Appl.* **9**, 034022 (2018).
32. Shang, Z. et al. Microwave-assisted spectroscopy of vacancy-related spin centers in hexagonal SiC. *Phys. Rev. Appl.* **15**, 034059 (2021).
33. Simin, D. et al. All-optical dc nanotesla magnetometry using silicon vacancy fine structure in isotopically purified silicon carbide. *Phys. Rev. X* **6**, 031014 (2016).
34. Landau, L. & Lifshitz, E. *Quantum Mechanics: Non-Relativistic Theory* (Elsevier Science, 2013).
35. Bir, G. & Pikus, G. *Symmetry and Strain-induced Effects in Semiconductors* (Wiley, 1974).
36. Lowdin, P.-O. A note on the quantum mechanical perturbation theory. *J. Chem. Phys.* **19**, 1396 (1951).
37. Udvarhelyi, P. et al. Vibronic states and their effect on the temperature and strain dependence of silicon-vacancy qubits in 4H- SiC. *Phys. Rev. Appl.* **13**, 054017 (2020).
38. Anisimov, A. N. et al. Optical thermometry based on level anticrossing in silicon carbide. *Sci. Rep.* **6**, 33301 (2016).
39. Anisimov, A. N. et al. Room-temperature level anticrossing and cross-relaxation spectroscopy of spin color centers in SiC single crystals and nanostructures. *Appl. Magn. Reson.* **49**, 85–95 (2018).
40. Tarasenko, S. A. et al. Spin and optical properties of silicon vacancies in silicon carbide—a review. *Phys. Status Solidi B Basic Res.* **255**, 1700258 (2018).
41. Sosnovsky, D. V. & Ivanov, K. L. Level-crossing induced spin phenomena in sic: a theoretical study. *Phys. Rev. B* **103**, 014403 (2021).
42. Dong, W., Doherty, M. W. & Economou, S. E. Spin polarization through intersystem crossing in the silicon vacancy of silicon carbide. *Phys. Rev. B* **99**, 184102 (2019).
43. Breev, I. D. et al. Stress-controlled zero-field spin splitting in silicon carbide. *Appl. Phys. Lett.* **118**, 084003 (2021).
44. Singh, H. et al. Experimental characterization of spin-$\frac{3}{2}$ silicon vacancy centers in 6*h*-sic. *Phys. Rev. B* **101**, 134110 (2020).
45. Singh, H., Anisimov, A. N., Breev, I. D., Baranov, P. G. & Suter, D. Optical spin initialization of spin-$\frac{3}{2}$ silicon vacancy centers in $6h-\mathrm{SiC}$ at room temperature. *Phys. Rev. B* **103**, 104103 (2021).
46. Soltamov, V. A. et al. Relaxation processes and high-field coherent spin manipulation in color center ensembles in 6h-sic. *Phys. Rev. B* **103**, 195201 (2021).
47. Astakhov, G. V. et al. Definitive observation of the dark triplet ground state of charged excitons in high magnetic fields. *Phys. Rev. B* **71**, 201312 (2005).
48. Togan, E. et al. Quantum entanglement between an optical photon and a solid-state spin qubit. *Nature* **466**, 730–734 (2010).
49. Anderson, C. P. et al. Electrical and optical control of single spins integrated in scalable semiconductor devices. *Science* **366**, 1225–1230 (2019).

ACKNOWLEDGEMENTS

The work was supported by the Russian Foundation for Basic Research, grant Nr. 19-52-12058 as well as by the Deutsche Forschungsgemeinschaft (DFG) grant No. AS 310/5-1 and in the framework of ICRC, project TRR 160 (Project No. C7). A.V.P. acknowledges the support from the Russian President Grant No. MK-4191.2021.1.2 and the Foundation "BASIS". Z.S. thanks support from the China Scholarship Council (CSC File No.: 201706220060). The study of ES fine structure was supported by the Russian Science Foundation grant 19-12-00051. The theory of temperature-dependent ODMR was supported by the Russian Science Foundation grant 21-72-10035. The research was partly supported by the state task of the Russian Federation No. FSRU-2021-0008.We thank Manfred Helm for encouragement.

AUTHOR CONTRIBUTIONS

I.D.B., Z.S., Y.B., and M.H. performed spectroscopic characterization and angular-dependence measurements. R.A.B., P.G.B., and A.N.A. performed ODMR, EPR, LAC spectroscopy. H.S. and D.S. performed pulse and CW ODMR at helium temperatures. A.V.P. and S.A.T. performed theoretical analysis. E.N.M. and S.S.N. performed sample growth, post-growth preparation, analysis of the structural and chemical quality of the crystal. A.N.A., A.V.P., S.A.T., I.D.B., Z.S., and G.V.A. analyzed the experimental data. A.V.P., S.A.T., G.V.A., and A.N.A. wrote the manuscript with input of all coauthors.

COMPETING INTERESTS

The authors declare no competing interests.

ADDITIONAL INFORMATION

Supplementary information The online version contains supplementary material available at https://doi.org/10.1038/s41534-022-00534-2.

Correspondence and requests for materials should be addressed to G. V. Astakhov or A. N. Anisimov.